Supplementary material

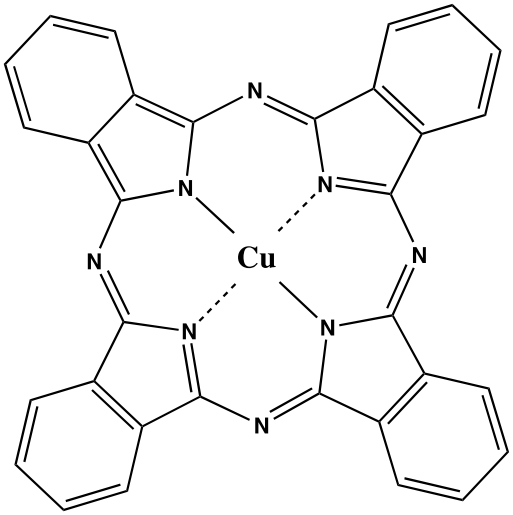

Figure S1. Schematic structure of CuPc.

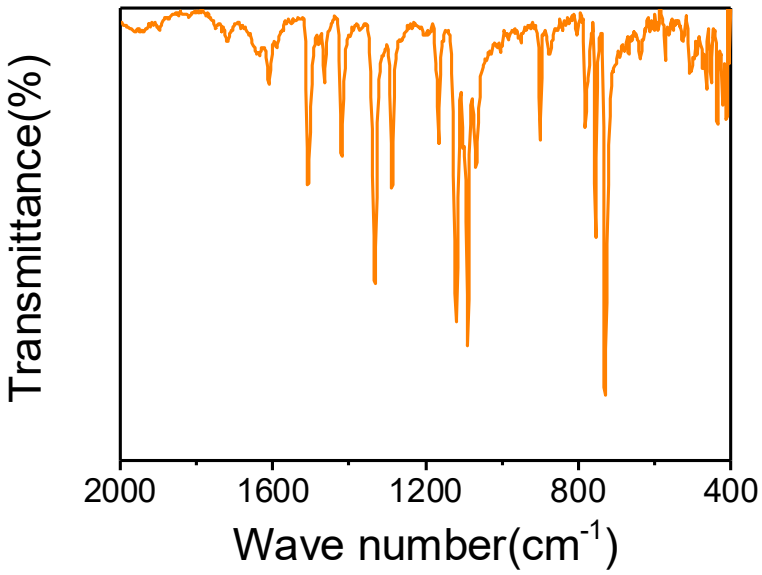

Figure S2. FTIR spectrum of the CuPc powder.

Figure S2 shows the Fourier infrared spectrum of CuPc[1]. The structure of CuPc includes the six-membered ring of benzene and the five-membered ring of pyrrole. In 572 cm^{-1}, 771 cm^{-1}, 864 cm^{-1}, 900 cm^{-1}, 1068 cm^{-1}, 1091 cm^{-1} and 1121 cm^{-1} peaks can be allocated to five-membered ring vibration peaks of pyrrole. The peaks at position 723 cm^{-1}, 754 cm^{-1}, 1508 cm^{-1}, 1610 cm^{-1} can be attributed to the six-membered ring vibration peaks of benzene. 1167 cm^{-1} is the vibration peak of the copper atom in the center coordinate the neighboring nitrogen atom, 1286 cm^{-1} and 1332 cm^{-1} can be attributed to the vibration peak of C=N-C.

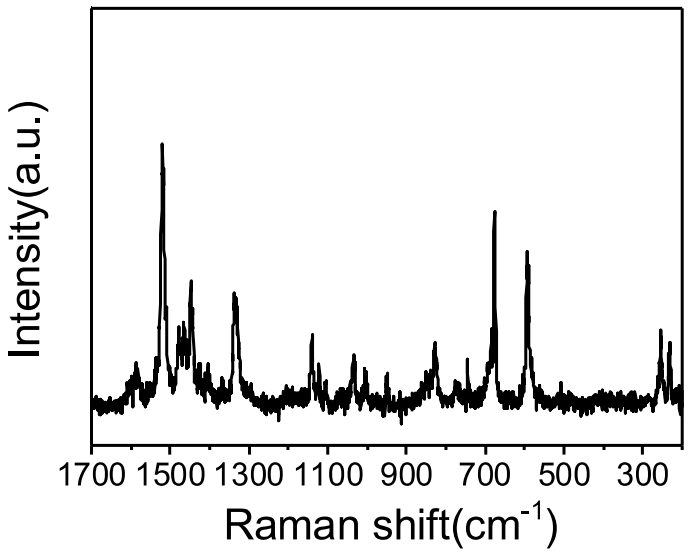

Figure S3. The Raman spectrum of the CuPc powder.

Figure S3 is Raman spectrum[2-6]. The bands in 1700-1200 cm^{-1} can be attributed to C=C or C=N/C-N vibration (1340 cm^{-1} refers to D-band and 1600 cm^{-1} refers to G-band,1430-1540 cm^{-1} refers to C=N/C-N), 1200-800 cm^{-1} can be attributed to C-H vibration. The strong vibration peak of 594 cm^{-1} is C-N-C, while the vibration peak of 682 cm^{-1} is C-C-H, and the vibration peak of 250 cm^{-1} is Cu-N vibration.

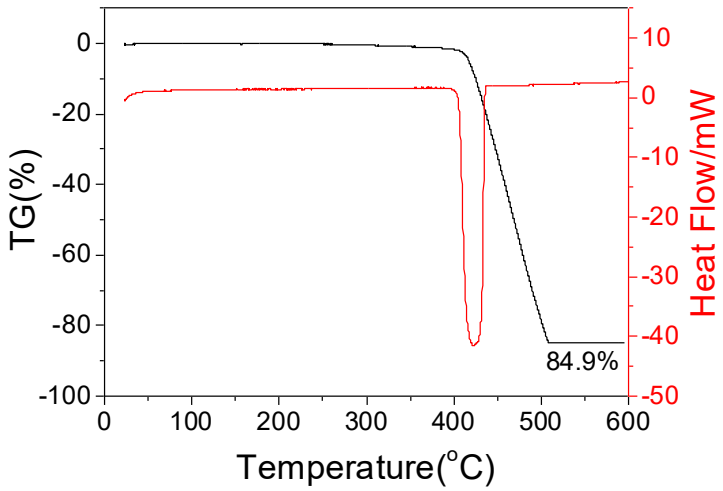

Figure S4. TG/DSC curves of the CuPc powder

Figure S4 shows the TG/DSC curve of the CuPc in air. The thermal properties of the material remain stable until 400 °C, no weight loss, heat absorption and heat release phenomena occur. When the temperature rises to about 415 °C, the material began to lose weight rapidly and eventually lost 84.9 % of its weight. According to the calculation of the final product as CuO, the theoretical weight loss is 86.19 %, which is basically consistent with the experimental results (84.9%). The high thermal stability of the CuPc ensures its high safety used as the electrode material under conditions such as thermal runaway.

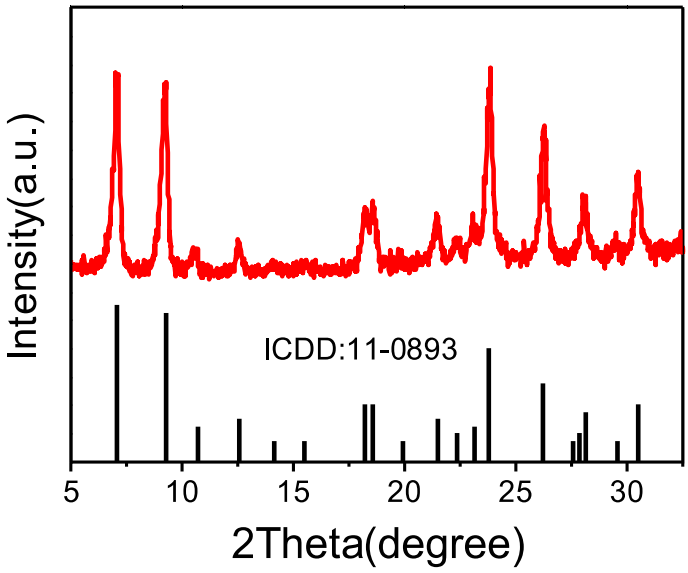

Figure S5. XRD patterns of the CuPc powder.

Figure S5 shows the XRD pattern of CuPc, which is in good consistency with the data of CuPc standard card (ICDD card no. 11-0893)[7, 8]. The space group of CuPc is $P2_1/a$. The copper atom is located at the center of the structure, in which four five-element rings contain four nitrogen atoms. The copper atom forms two covalent bonds with two of these four nitrogen atoms and two coordination bonds with the other two nitrogen atoms (see **Figure S1**).

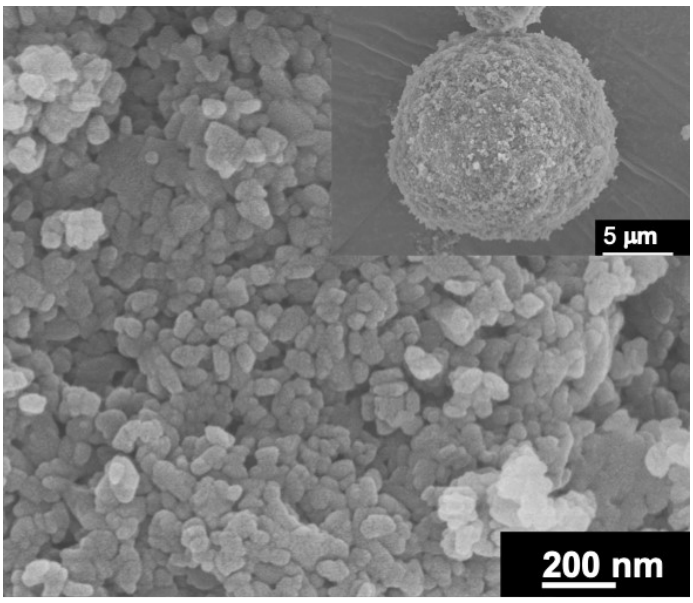

Figure S6. SEM images of the CuPc powder.

Figure S6 is a scanning electron microscope image of CuPc. The scanning electron microscope (SEM) image of CuPc at low-magnification (insert) showed that the morphology was flocculent spherical particles with a diameter of about 18μm. From the high-magnification images, it is clear that the spherical shape particles are composed of smaller particles (about 50 nm).

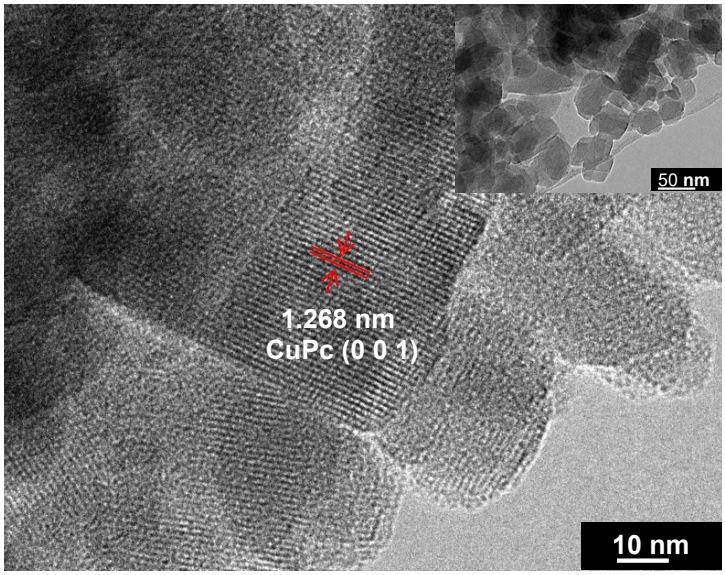

Figure S7. TEM images of the CuPc powder.

HRTEM image shown in **Figure S7** exhibits clear lattice pattern, indicating the fringe spacing is measured to be 1.268 nm, corresponding to the inter planar spacing of (001) plane of CuPc. The nanoscale of the materials can shorten the transport path of ion in electrochemical reactions. On the other hand, the gap between the nanoparticles is favorable for the sufficient infiltration of the electrolyte. Both of above can be help to improve the rate capability of the electrode material.

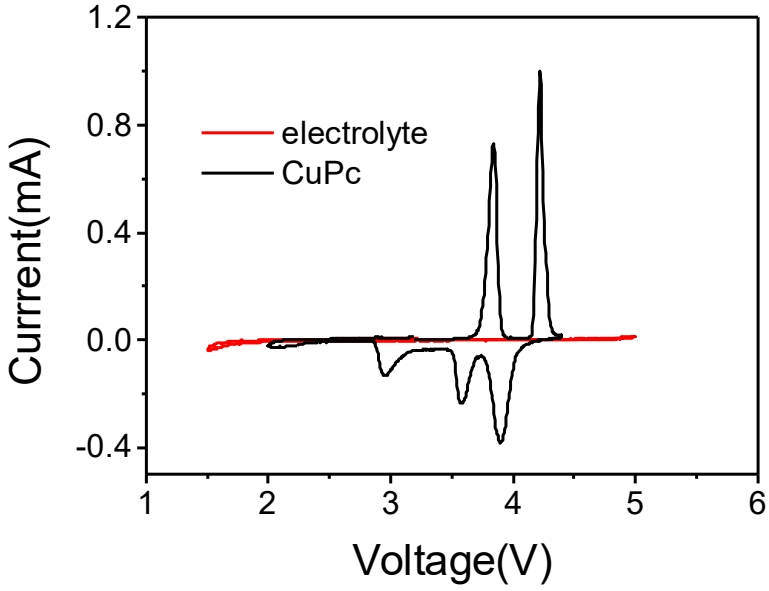

Figure S8. CV curves of electrolyte (red, HFE:FEMC:FEC=1:2:1) and CuPc cathode material at 0.5 mV s^{-1}.

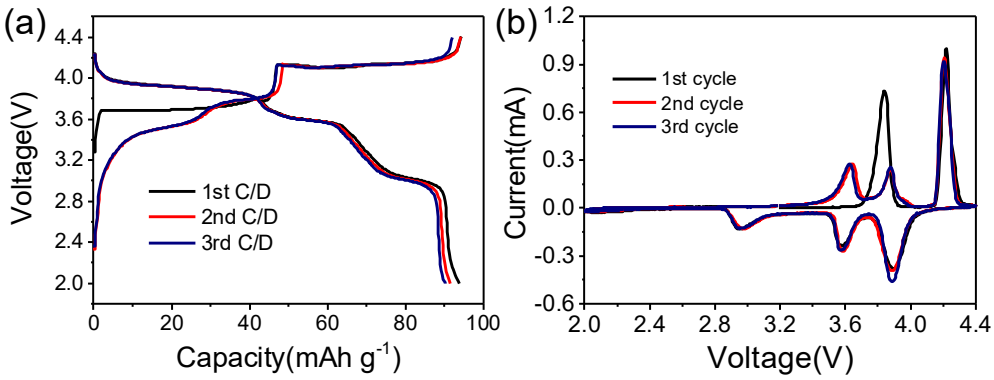

Figure S9. Electrochemical performance of CuPc as the cathode material: (a) the charge-discharge curves in the first three cycles (100 mA g^{-1}), (b) the CV curves in the first three cycles (0.5 mV s^{-1}) .

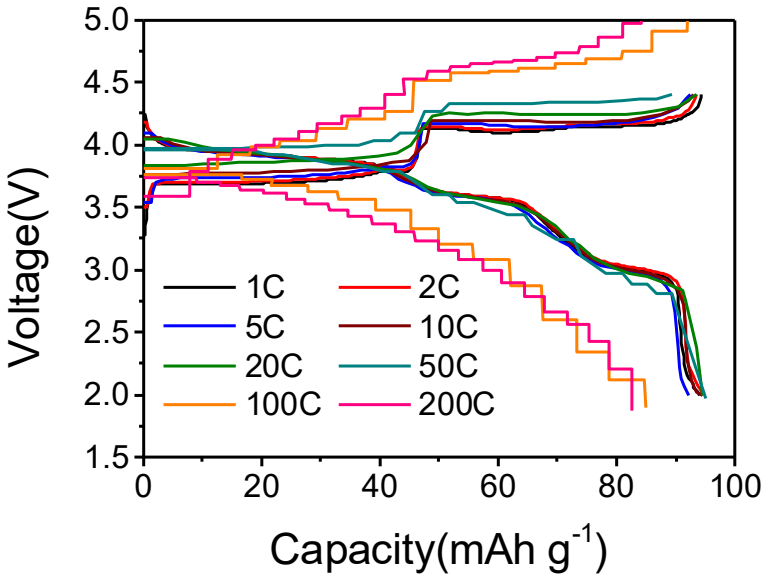

Figure S10. Charge/discharge curves of the first cycle at different rates (Considering the polarization phenomenon, in order to reflect the second charging plateau, the charging termination voltage is set at 5.0 V when the current density is 100C and 200C).

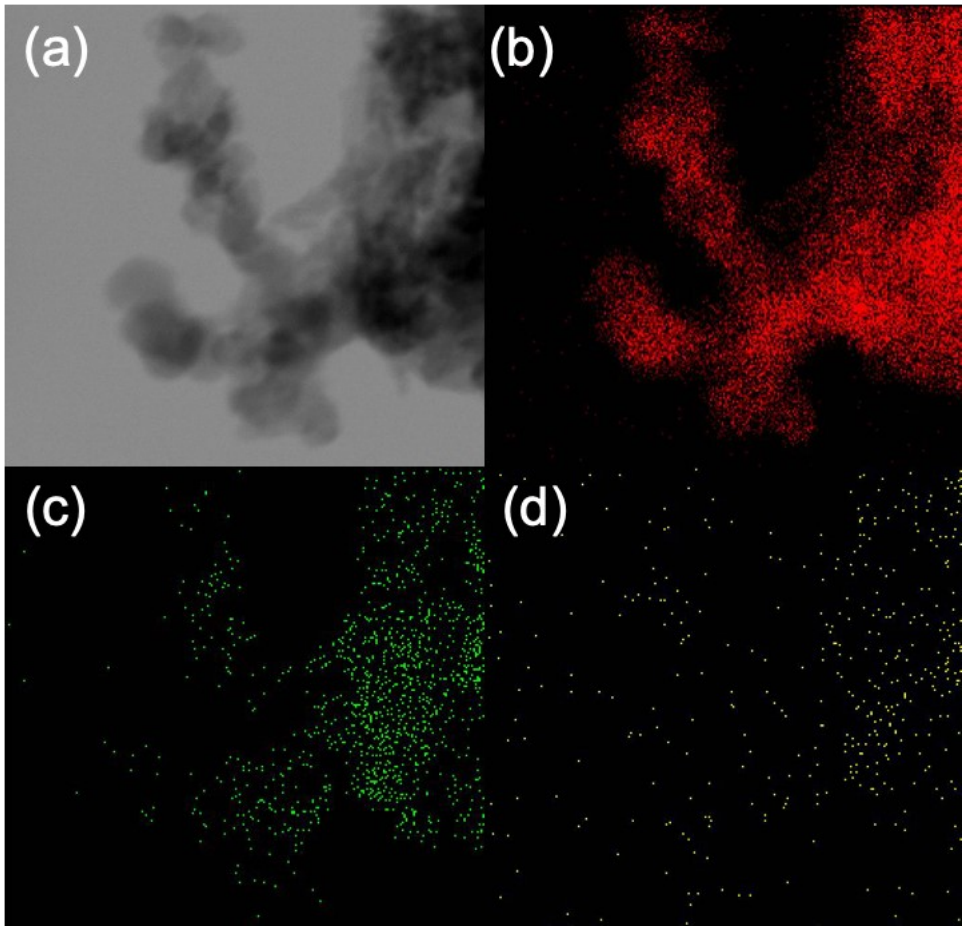

Figure S11. The elemental mapping images of the CuPc electrode charged to 4.4 V (a) dark-field scanning transmission electron microscopy, (b) C, (c) N, (d) Cu.

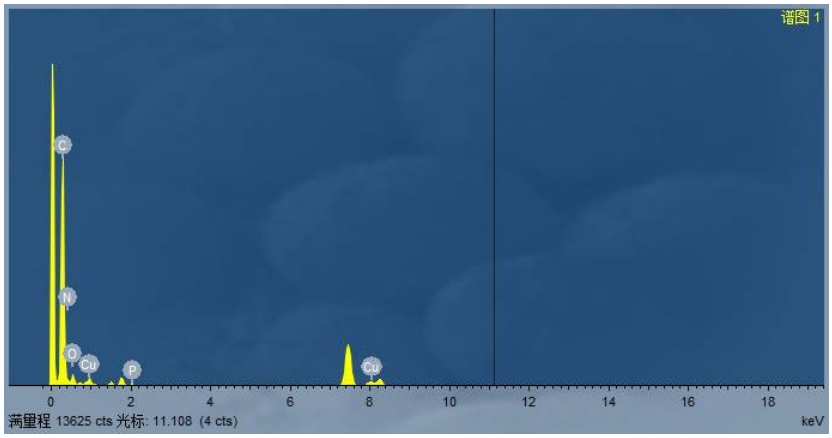

Figure S12. The elemental contents of the CuPc electrode charged to 4.4 V.

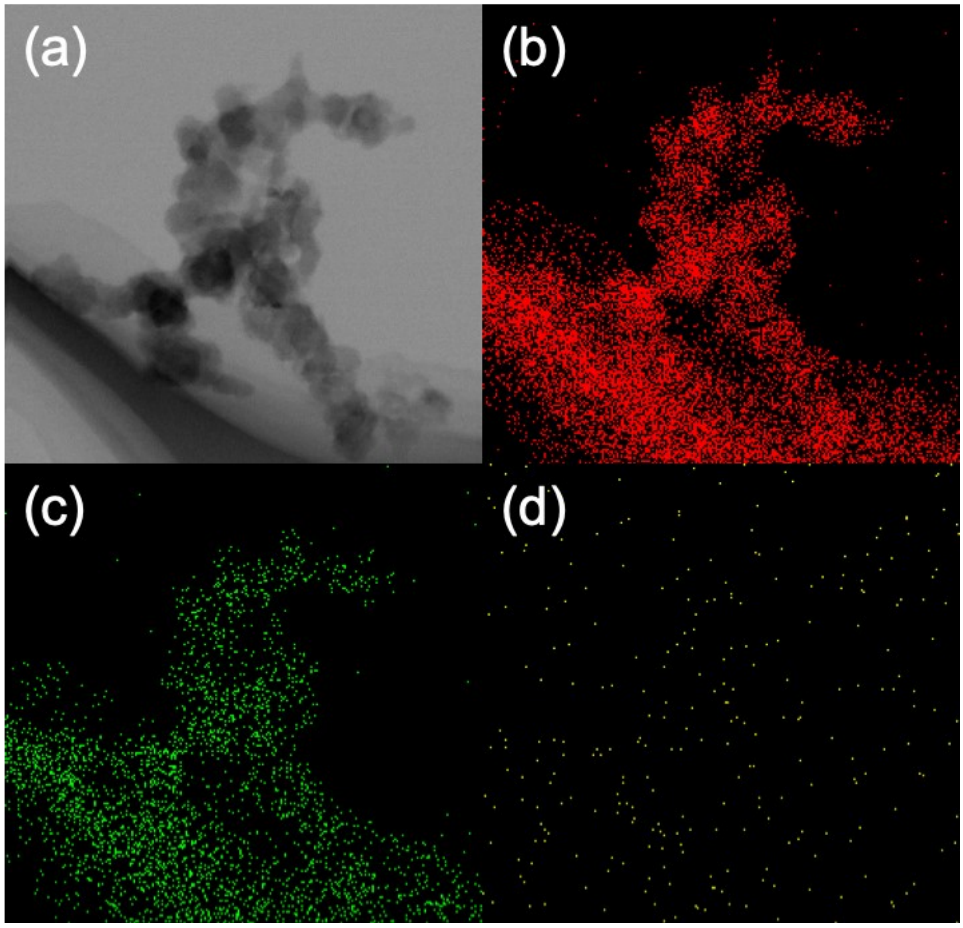

Figure S13. The elemental mapping images of the CuPc electrode discharged to 2.0 V (a) dark-field scanning transmission electron microscopy, (b) C, (c) N, (d) Cu.

Figure S14. The elemental contents of the CuPc electrode discharged to 2.0 V.

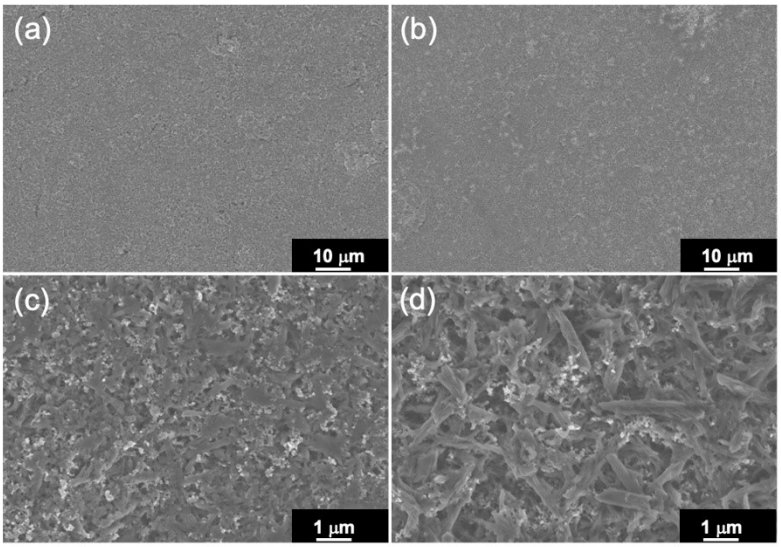

Figure S15. SEM images of the CuPc electrode. (a) pristine electrode, (b) after charge/discharge cycles, (c) charged state (after charge/discharge cycles), (d) discharged state (after charge/discharge cycles).

The SEM images of the CuPc electrodes before and after charge/discharge cycles in Figure S15 (a) and (b) show that the surface of the electrodes is uniform and flat. The SEM images of CuPc electrodes at different states after the charge/discharge cycles in Figure S15 (c) and (d) show that CuPc can always maintain the polymerization state, indicating that the electrodes keep stable and CuPc is in polymerization state during the charge/discharge cycles.

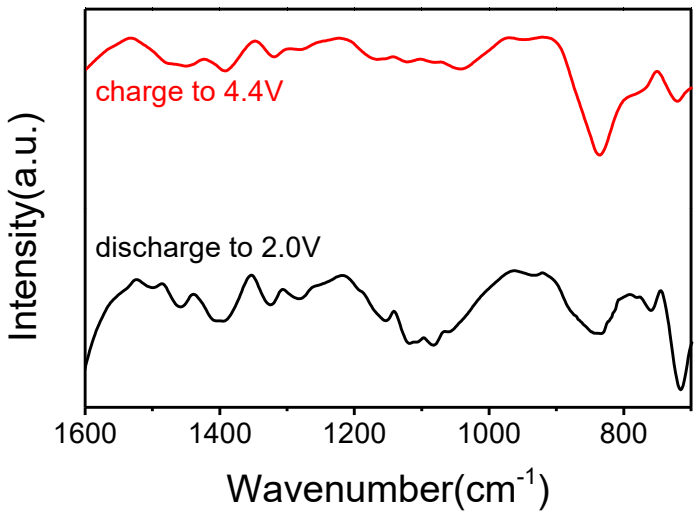

Figure S16. FTIR spectra of the CuPc electrodes at different states after charge/discharge cycles.

The FTIR spectrum of CuPc at different states after charge/discharge cycles still show the characteristic peak of benzene ring polymerization at 838 cm^{-1}, which indicates that CuPc can always keep the stable polymerization state.

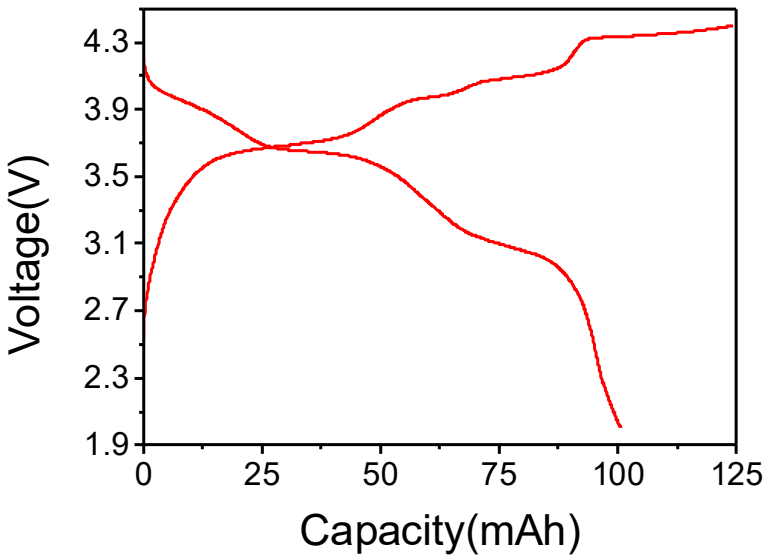

Figure S17. Charge/discharge curves of CuPc/Li battery in the first cycle (1C).

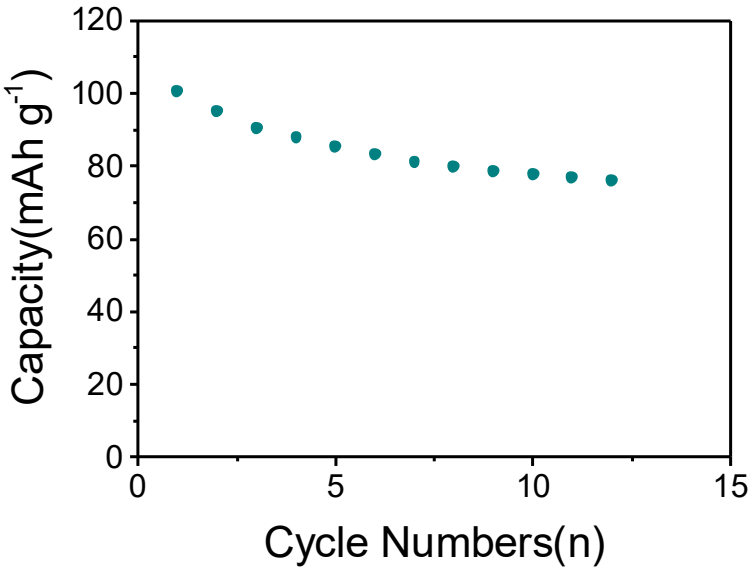

Figure S18. The cycling performance of CuPc/Li battery (1C).

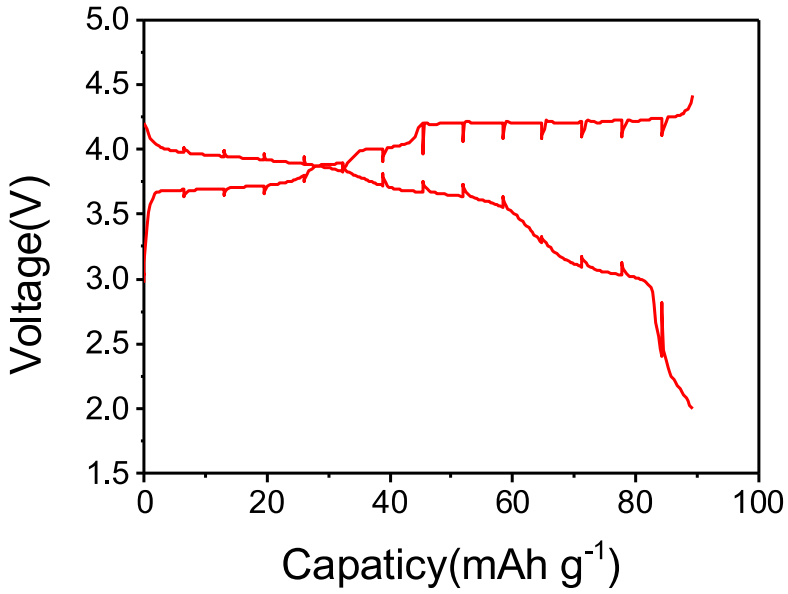

Figure S19. The GITT curves of CuPc electrode.

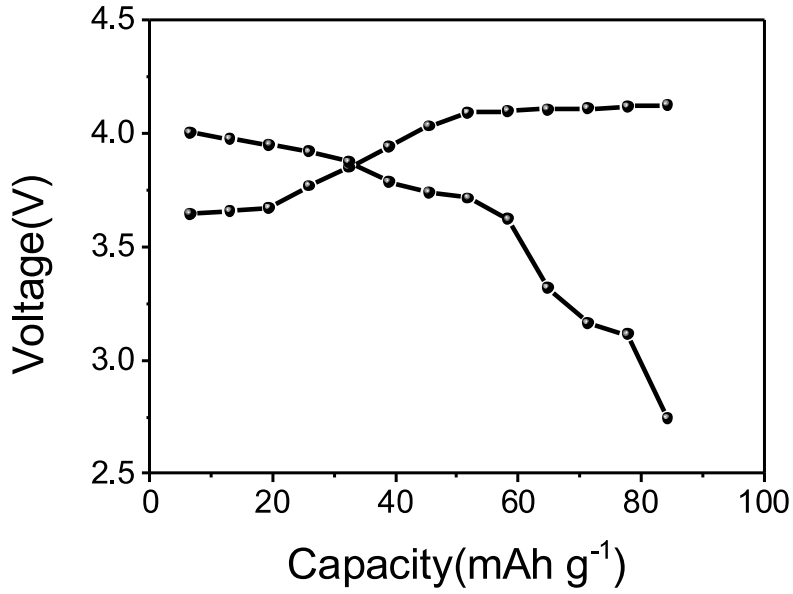

Figure S20. Equilibrium potential versus specific capacity during GITT measurement.

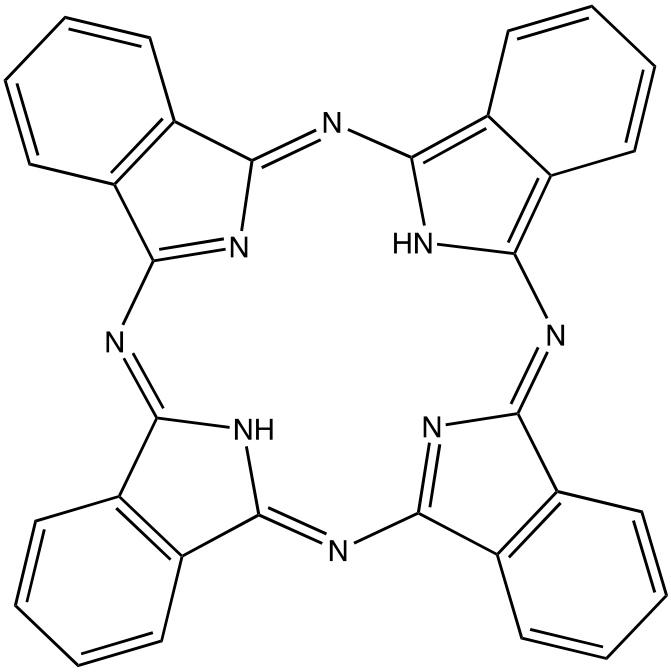

Figure S21. Schematic structure of Pc.

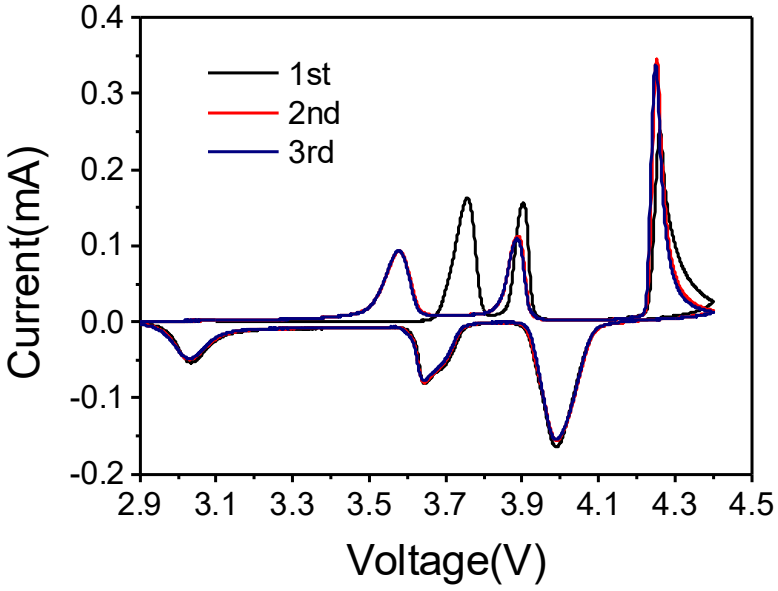

Figure S22. CV curves in the first three cycles (0.1 mV s^{-1}) of Pc.

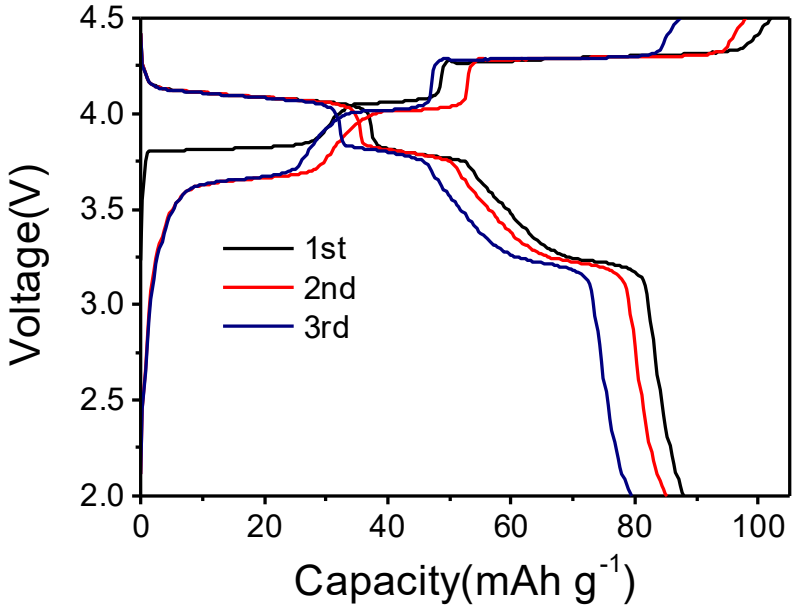

Figure S23. The charge-discharge curves of Pc electrode in the first three cycles(10 mA g^{-1}).

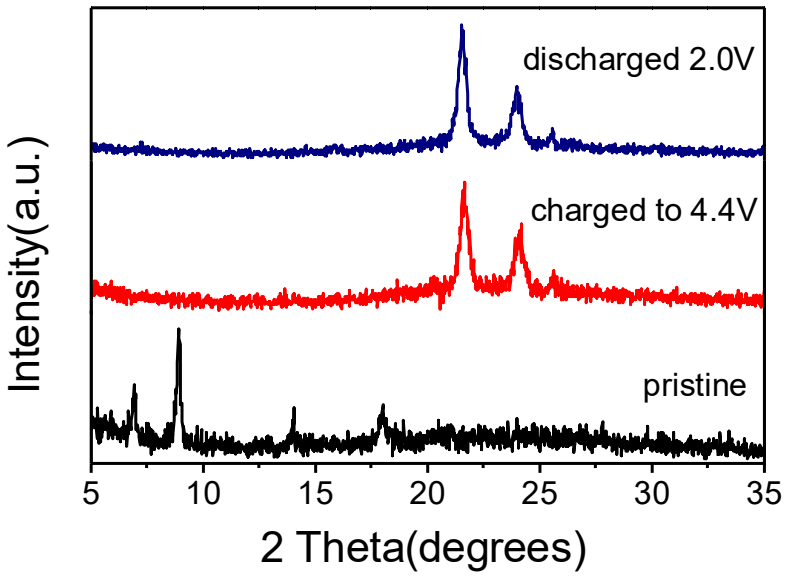

Figure S24. XRD patterns of Pc electrodes at different states.

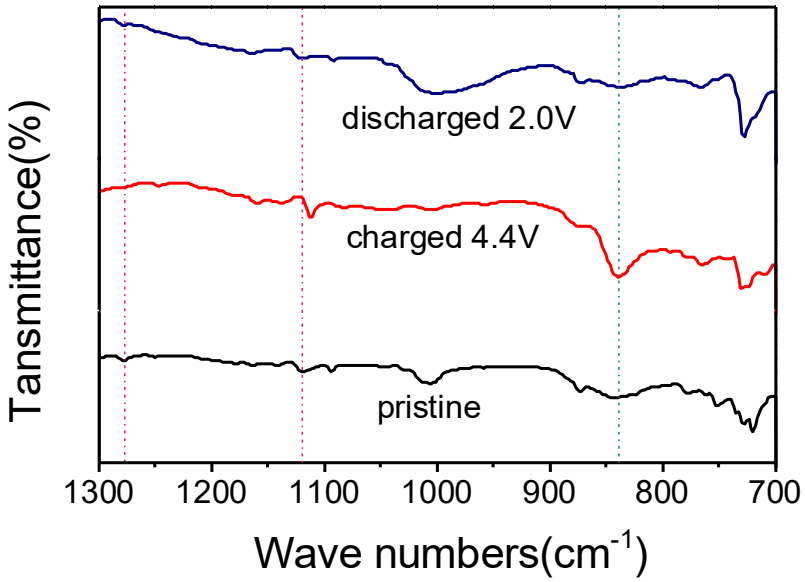

Figure S25. FTIR spectra of Pc electrodes at different states.

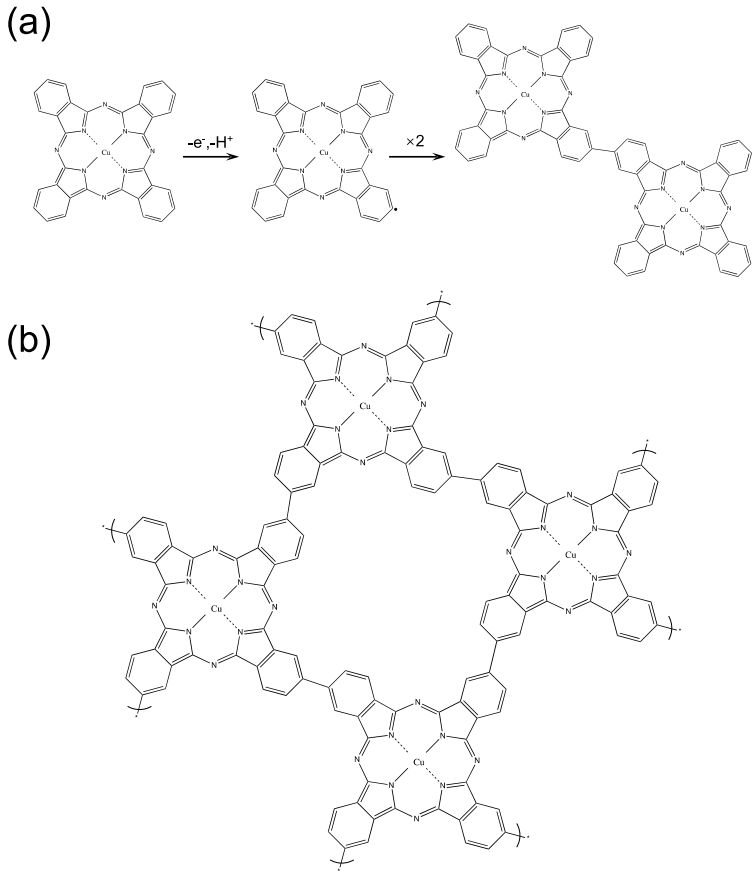

Figure S26. (a) Self-polymerization reaction mechanism of CuPc (take two CuPc units as an example), (b) Schematic structure of poly-CuPc.

Referring to some other studies[9-13], we speculate that the polymerization mechanism of CuPc may be are: Firstly, the benzene ring is catalyzed by divalent copper ion to generate free radicals, and then CuPcs are oxidized to form polymerized CuPc (**Figure S26**(a)).

Table S1. The rate performance comparison of Inorganic and organic cathode materials

Cathode materials	Structural formula	Rate (C)	Capacity (mAh g^{-1})	Ref.
Inorganic materials	NCM(622)	10C (0.5C charge)	151	14
	NCM(811)	10C	134	15
	NCM (811)	20C	118	16
	NMC(111)	20C	138	17
		30C	131	17
	NMC(111)	20C	137	18
	$LiCoO_2$	10C	142	19
	$LiCoO_2$ (Thin Film)	100C	60	20
	$LiMn_2O_4$	9C	45	21
	$LiMn_2O_4$	10C	94.7	22
	$LiFePO_4$	150C	95.4	23
	$LiFePO_4$	200C	78	24
Organic materials	p-DPPZS	10C	95	25
		20C	64	25
	P1a	100C	32.7	26
	TCTA	20A/g(~200C)	38	27
	PDPPD	100C	84	28
	PVMPT	100C	26	29
	p-DPPZ	5C	65	30
	CuPc	5C	93.4	this work
		10C	93.3	this work
		20C	92.8	this work
		50C	91.2	this work
		100C	84.9	this work
		200C	82.7	this work

Table S2. Impedance parameters of CuPc cell with different cycle numbers.

Cycle number	0	10	50	80	200	500	1000
R_s (Ω)	4.42	4.88	7.56	6.4	7.38	6.64	9.44
R_{ct} (Ω)	204.98	40.85	31.35	35.80	36.42	34.86	44.46

R_s series ohmic resistances.

R_{ct} charge transfer resistances.

References

1. L. B. C. Medhat A. Shaibat, Diana Y. Siberio-Pe´rez, Adam J. Matzger, and and Y. Ishii, J. Phys. Chem. B, 2010, 114, 7.
2. T. V. B. a. B. A. Kolesov, Journal of Structural Chemistry, 2000, 41, 8.
3. T. V. Basova, V. G. Kiselev, B.-E. Schuster, H. Peisert and T. ChassÃ, Journal of Raman Spectroscopy, 2009, 40, 2080-2087.
4. F. Cerdeira, M. Garriga, M. I. Alonso, J. O. Ossó, F. Schreiber, H. Dosch and M. Cardona, Journal of Raman Spectroscopy, 2013, 44, 597-607.
5. P. Zhang, M. Wang, Y. Liu, S. Yang, F. Wang, Y. Li, G. Chen, Z. Li, G. Wang, M. Zhu, R. Dong, M. Yu, O. G. Schmidt and X. Feng, Journal of the American Chemical Society, 2021, 143, 10168-10176.
6. H. Zhong, M. Ghorbani-Asl, K. H. Ly, J. Zhang, J. Ge, M. Wang, Z. Liao, D. Makarov, E. Zschech, E. Brunner, I. M. Weidinger, J. Zhang, A. V. Krasheninnikov, S. Kaskel, R. Dong and X. Feng, Nature Communications, 2020, 11, 1409.
7. C. J. Brown, J. Chem. SOC. (A), 1968, 6.
8. M. T. Hussein, K. A. Aadim and E. K. Hassan, Advances in Materials Physics and Chemistry, 2016, 06, 85-97.
9. A. E. Wendlandt, A. M. Suess and S. S. Stahl, Angewandte Chemie International Edition, 2011, 50, 11062-11087.
10. M. Kitahara, N. Umeda, K. Hirano, T. Satoh and M. Miura, Journal of the American Chemical Society, 2011, 133, 2160-2162.
11. K. V. N. Esguerra, Y. Fall, L. Petitjean and J.-P. Lumb, Journal of the American Chemical Society, 2014, 136, 7662-7668.
12. X. Li, J. B. Hewgley, C. A. Mulrooney, J. Yang and M. C. Kozlowski, The Journal of Organic Chemistry, 2003, 68, 5500-5511.
13. T. Kijchavengkul, R. Auras, M. Rubino, M. Ngouajio and R. T. Fernandez, Chemosphere, 2008, 71, 942-953.
14. S. Kalluri, H. Cha, J. Kim, H. Lee, H. Jang and J. Cho, Advanced Science, 2020, 7, 1902844.
15. S. Wang, A. Dai, Y. Cao, H. Yang, A. Khalil, J. Lu, H. Li and X. Ai, Journal of Materials Chemistry A, 2021, 9, 11623-11631.
16. F. Cheng, X. Zhang, Y. Qiu, J. Zhang, Y. Liu, P. Wei, M. Ou, S. Sun, Y. Xu, Q. Li, C. Fang, J. Han and Y. Huang, Nano Energy, 2021, 88, 106301.
17. D. Ren, E. Padgett, Y. Yang, L. Shen, Y. Shen, B. D. A. Levin, Y. Yu, F. J. DiSalvo, D. A. Muller and H. D. Abruña, ACS Applied Materials & Interfaces, 2019, 11, 41178-41187.
18. J. Li, X. Wang, J. Zhao, J. Chen, T. Jia and C. Cao, Journal of Power Sources, 2016, 307, 731-737.
19. L. Wang, J. Ma, C. Wang, X. Yu, R. Liu, F. Jiang, X. Sun, A. Du, X. Zhou and G. Cui, Advanced Science, 2019, 6, 1900355.
20. S. Yasuhara, S. Yasui, T. Teranishi, K. Chajima, Y. Yoshikawa, Y. Majima, T. Taniyama and M. Itoh, Nano Letters, 2019, 19, 1688-1694.
21. J. Abou-Rjeily, I. Bezza, N. A. Laziz, C. Autret-Lambert, M. T. Sougrati and F. Ghamouss, Energy Storage

Materials, 2020, 26, 423-432.
22. Y. Qiao, S.-R. Li, Y. Yu and C.-H. Chen, Journal of Materials Chemistry A, 2013, 1, 860-867.
23. H. Wang, R. Wang, L. Liu, S. Jiang, L. Ni, X. Bie, X. Yang, J. Hu, Z. Wang, H. Chen, L. Zhu, D. Zhang, Y. Wei, Z. Zhang, S. Qiu and F. Pan, Nano Energy, 2017, 39, 346-354.
24. B. Wang, Y. Xie, T. Liu, H. Luo, B. Wang, C. Wang, L. Wang, D. Wang, S. Dou and Y. Zhou, Nano Energy, 2017, 42, 363-372.
25. G. Dai, Y. Liu, Z. Niu, P. He, Y. Zhao, X. Zhang and H. Zhou, Matter, 2019, 1, 945-958.
26. P. Acker, L. Rzesny, C. F. N. Marchiori, C. M. Araujo and B. Esser, Advanced Functional Materials, 2019, 29, 1906436.
27. C. Zhao, Z. Chen, W. Wang, P. Xiong, B. Li, M. Li, J. Yang and Y. Xu, Angew Chem Int Ed Engl, 2020, 59, 11992-11998.
28. F. A. Obrezkov, A. F. Shestakov, V. F. Traven, K. J. Stevenson and P. A. Troshin, Journal of Materials Chemistry A, 2019, 7, 11430-11437.
29. M. Kolek, F. Otteny, P. Schmidt, C. Mück-Lichtenfeld, C. Einholz, J. Becking, E. Schleicher, M. Winter, P. Bieker and B. Esser, Energy & Environmental Science, 2017, 10, 2334-2341.
30. G. Dai, X. Wang, Y. Qian, Z. Niu, X. Zhu, J. Ye, Y. Zhao and X. Zhang, Energy Storage Materials, 2019, 16, 236-242.